# Cryo-EM structure of a monomeric yeast *S. cerevisiae* complex IV isolated with maltosides: Implications in supercomplex formation

Gabriel Ing [a], Andrew M. Hartley [b], Nikos Pinotsis [b], Amandine Maréchal [a,b,*]

[a] *Institute of Structural and Molecular Biology, University College London, Gower Street, London WC1E 6BT, UK*
[b] *Institute of Structural and Molecular Biology, Birkbeck College, Malet Street, London WC1E 7HX, UK*

## ARTICLE INFO

## ABSTRACT

In mitochondria, complex IV (CIV) can be found as a monomer, a dimer or in association with other respiratory complexes. The atomic structure of the yeast *S. cerevisiae* CIV in a supercomplex (SC) with complex III (CIII) pointed to a region of significant conformational changes compared to the homologous mammalian CIV structures. These changes involved the matrix side domain of Cox5A at the CIII-CIV interface, and it was suggested that it could be required for SC formation. To investigate this, we solved the structure of the isolated monomeric CIV from *S. cerevisiae* stabilised in amphipol A8–35 at 3.9 Å using cryo-electron microscopy. Only a minor change in flexibility was seen in this Cox5A region, ruling out large CIV conformational shift for interaction with CIII and confirming the different fold of the yeast Cox5A subunit compared to mammalian homologues. Other differences in structure were the absence of two canonical subunits, Cox12 and Cox13, as well as Cox26, which is unique to the yeast CIV. Their absence is most likely due to the protein purification protocol used to isolate CIV from the III-IV SC.

## 1. Introduction

Cytochrome *c* oxidase or respiratory complex IV (CIV) performs the last step in the mitochondrial respiratory electron transport chain. CIV catalyses the reduction of molecular oxygen into two water molecules, with four electrons from the oxidation of four reduced cytochrome *c*, and four substrate protons taken from the mitochondrial matrix. In addition, CIV pumps four additional protons across the inner mitochondrial membrane, from the matrix to the inter-membrane space, contributing to the electrochemical proton gradient which is used to drive ATP synthesis [1].

CIV is a multi-subunit enzyme, and up to 14 subunits have been identified in the human CIV [2]. The three core catalytic subunits (subunits COX1–3) are encoded by the mitochondrial genome, and the other eleven, by the nuclear DNA. COX1–3 are highly conserved in all cytochrome *c* oxidases. They contain the key catalytic elements of the enzyme including: the haem and copper cofactors required for electron transfer and oxygen chemistry, the hydrophilic pathways that allow proton transfers within the protein hydrophobic core, and the channel for oxygen delivery to the active site. The nuclear subunits, also called

'accessory' or 'supernumerary' subunits, govern other features of CIV, including assembly, stability, association with other respiratory complexes to form supercomplexes (SCs) and, potentially, regulation of the catalytic processes *via* mechanisms which remain to be fully understood [3].

For many years, the only structural information available at atomic resolution on mitochondrial complex IV were dimeric crystal structures of the bovine enzyme, the first one being published in 1996 [4]. However, the furthering of our understanding of CIV membrane organisation and the use of milder detergent conditions have led, in recent years, to many new mitochondrial CIV structures. These include the X-ray structure of a monomeric bovine CIV [5] and the cryo-EM structures of CIV as part of the human megacomplex [2] and as part of a III-IV SC in the yeast *Saccharomyces cerevisiae* [6–8], plant *Vigna radiata* [9] and mouse/ovine [10].

The yeast *S. cerevisiae* has been extensively used to study the mitochondrial electron transport chain proteins despite lacking complex I. This is thanks to the remarkable similarity of the yeast complexes II-V with mammalian homologues, and the unique ability to mutate yeast mitochondrial DNA [11] to study the effect of mutations in the core

catalytic subunits and unravel the details of CIV molecular mechanism and regulation. Therefore, yeast studies can present new and useful information through genetic modification of core subunits, which when used in parallel with mammalian studies can yield findings relevant to human disease.

The first full atomic model of yeast *S. cerevisiae* CIV was obtained within the III-IV SC [6]. The structure revealed a complex assembly of 12 subunits and confirmed its overall similarity with mammalian CIV [12], in particular, the catalytic core of Cox1–3. Whilst the catalytic core closely resembled the mammalian homolog, key differences in the yeast CIV supernumerary subunits were highlighted including the presence of subunit Cox26 (unique to the yeast enzyme) and significant difference in structure of Cox13. Furthermore, the sole yeast CIV subunit making protein:protein interactions with CIII was subunit Cox5, homologous to mammalian COX4. Comparison of CIV within the yeast SC with available mammalian CIV structures showed a conformational change in Cox5 (yeast nomenclature) and we postulated that this could be required for SC formation or stability. In *S. cerevisiae*, CIV is always found in a SC with CIII but maltosides can be used to effectively dissociate the two complexes. In this study, CIV was isolated from yeast *S. cerevisiae* mitochondrial membranes using the detergent undecyl-maltoside (UDM). CIV was then stabilised in amphipols and the structure of monomeric CIV was determined to a nominal resolution of 3.9 Å by cryo-electron microscopy (cryo-EM). The structure obtained for this yeast monomeric CIV is discussed in comparison to the yeast CIV structure derived from the yeast III-IV SC as well as with other available mammalian CIV structures.

## 2. Material and methods

### 2.1. Cell growth, mitochondrial membrane preparation and purification of monomeric complex IV

The modification of yeast strain W303—1B to incorporate a 6-histidine tag sequence on the 3′ end of nuclear gene *cox13*, was described in Meunier et al. [13]. Cells were grown in baffled flasks in a YPGal (1 % yeast extract, 2 % peptone and 2 % galactose) medium with agitation and were harvested by centrifugation in late log phase. Mitochondrial membranes were prepared by differential centrifugation following mechanical cell disruption with a glass bead beater as previously described [13]. Membranes were diluted to a total protein content of 2 mg/ml in 50 mM HEPES, 150 mM NaCl, 0.1 mM PMSF/EtOH at pH 8.0, and solubilised by incubation for 1 h at 4 °C with 2 % *w/v* n-undecyl-β-D-maltoside (UDM, Anatrace). Unsolubilised material was pelleted by centrifugation at 120,000 $g_{av}$ for 35 min, 4 °C, and 10 mM imidazole and 350 mM NaCl were added to the supernatant before adjusting the pH to 8.0 and loading onto a pre-equilibrated Ni-NTA column operated by an Äkta Pure 25. The resin with bound CIV was washed with 4 column volumes of 50 mM HEPES, 500 mM NaCl, 10 mM imidazole and 0.2 % UDM at pH 8.0 and CIV was eluted with the same solution with increased imidazole concentration to 100 mM. 1 mM EDTA and 10 % ethylene glycol were added to the protein eluate before flash freezing and storage at −80 °C.

### 2.2. Amphipol exchange

The protein eluate was thawed and incubated with A8–35 (Anatrace) at a 10:1 amphipol:protein ratio for 30 min at 4 °C, with gentle agitation on a rotary shaker. To remove the remaining UDM, four batches of 400 mg BioBeads (Bio-Rad) were consecutively added to the amphipol:protein mixture and left shaking for 1 h each, resulting in a total incubation time of 4 h. The protein was then applied to a Superose 6 Increase column pre-equilibrated with 50 mM HEPES, 150 mM NaCl, pH 7.2, and the elution peak corresponding to complex IV was then collected, concentrated using 100 kDa MWCO centrifugal concentrators, and re-applied to the same column. The purity of the resulting CIV was

confirmed by sodium dithionite-reduced *minus* oxidised difference absorption spectra recorded in the visible range. The concentration in CIV was determined using an extinction coefficient of 26 mM$^{-1}$·cm$^{-1}$ at ΔA 603–621 nm.

### 2.3. Activity measurements

Turnover numbers of CIV were determined from oxygen consumption rates using a Clark-type polarographic oxygen electrode (Oxygraph+, Hansatech Instruments Ltd). Assays were conducted at 25 °C in a 1 ml reaction vessel containing 5 nmol CIV diluted in 10 mM KPi, 50 mM KCl, 0.05 % UDM, pH 6.6, and supplemented with 40 μM TMPD and 2 mM sodium ascorbate. The reaction was initiated by addition of 50 μM horse heart cytochrome *c*. The result presented is the average of three measurements (±s.d.).

### 2.4. Preparation of cryo-EM grids and data acquisition

Purified CIV stabilised in A8–35 (5 μM) was diluted 1:3 in 50 mM HEPES, 150 mM NaCl, pH 7.2, and applied to glow-discharged UltrAuFoil R1.2/1.3 grids (Quantifoil). The grid was blotted using a Vitrobot Mark IV (Thermo Fisher) for 12 s at 4 °C and 90 % humidity, and plunged in liquid ethane. Grids were stored in liquid nitrogen until required. Data collection was performed using a Titan Krios microscope (Thermo Fisher) equipped with a K2 Summit direct electron detector (Gatan) (Birkbeck College, UK), at a magnification of ×165,000, corresponding to a pixel size of 0.82 Å. The sample was exposed to a dose rate of 7.99 e$^-$/Å/s and a total dose of 47.9 e$^-$/Å split into 30 frames per movie. In total 4292 movies were collected in counting mode using the EPU software (Thermo Fisher) with a defocus range of −1.4 to −3.0 μm.

### 2.5. Image processing

The movie frames were motion corrected by MotionCor2 [14] as implemented in Relion3.1 [15]. The dose weighted images were then imported to CryoSPARCv2 [16] where all of the following processes were performed. The CCTFIND4 software [17] was used for the estimation of the contrast transfer function (CTF) resulting in the rejection of 152 images with significant CTF decay, due to image drift, thick ice, or other defects. 970 particles were then picked manually across 96 images followed by 2D classification. The best eight 2D classes were used as templates for the template picker job in cryoSPARCv2. This gave 598,022 particles which were extracted and used for *ab initio* 3D reconstruction generating four 3D classes. Particles from two of these classes were combined for heterogeneous 3D refinement generating 5 models; one at an estimated resolution 4.69 Å and the other four at around 7.9 Å. Particles from three of these models were combined for a second round of heterogeneous refinement that gave a main model at 4.95 Å from 77,428 particles.

To further improve the model quality these particles were used for a new 2D classification. 25 out of 30 2D classes were selected comprising a total of 72,409 particles. These were used for a final round of non-uniform refinement that gave a map with an estimated resolution 3.87 Å based on the gold standard Fourier shell correlation (FSC) curve with a cut off value of 0.143 (Supplementary Fig. S2). Supplementary Fig. S3 presents a flowchart of the image processing.

### 2.6. Model building

Model building was performed by running phenix.dock_in_map with chains a-i of the previously determined model of CIV in a SC with CIII (PDB-ID 6HU9) and phenix.real_space_refine to refine the structure [18]. The refinement was restrained against the secondary structure elements of CIV, Ramachandran angles and rotamers as well ligands and coordinated metals. Following each round of refinement the model was interpreted and manually corrected in Coot [19]. Model and map

validation was performed with phenix.mtriage and phenix.molprobity [18]. The model was compared to the previously published yeast SC structures (PDB IDs 6HU9, 6T15 and 6T0B) as well the bovine monomer (6JY3). PyMOL [20] and the PDBeFOLD server [21] were used for structural comparisons. PyMOL and UCSF Chimera [22] were used for figure preparation.

Data collection and refinement statistics are summarised in Supplementary Information Table S1. A list of all prosthetic groups and other ligands is given in Table S2.

## 3. Results and discussion

### 3.1. Purification of monomeric complex IV and amphipol exchange

Monomeric CIV was isolated from yeast mitochondrial membranes following solubilisation with UDM (see methods). Our own attempts to solve the cryo-EM structure of the enzyme in maltosides failed, primarily due to the presence of detergent micelles in the vitreous ice, a by-product of protein concentration. To circumvent this issue, amphipol exchange was used to gently remove the maltoside detergent from the protein prior to cryo-grid preparation. A8–35 is an amphipathic molecule that can be exchanged with detergents to enable stabilisation of membrane proteins in detergent-free solutions, and has been successfully used in the structural studies of very many membrane proteins [23], including respiratory complexes [24] and SCs [9,10]. After amphipol exchange and removal of UDM by BioBeads (see methods), the protein was further purified by size exclusion chromatography (Fig. SI 1A). The sodium dithionite reduced *minus* oxidised difference absorption spectrum recorded on the final CIV sample used for cryo-EM grids preparation displayed the characteristic redox signature of haem *a* and haem $a_3$ (Fig. SI 1B) indicating no disrupting effect of amphipol exchange on the co-factors environment and confirming the absence of CIII.

in the preparation. The CIV concentration was measured at 5.8 μM from the absorption of the α-band with maximum at 603 nm.

### 3.2. Cryo-EM structure of monomeric complex IV

Cryo-EM grids were prepared from the purified CIV stabilised in A8–35. Data collection and images processing are described in methods. The final cryo-EM map of the monomeric CIV comprises nine protein chains, Cox1 to 4, Cox5A and Cox6 to 9 (Fig. 1). Compared to the CIV structures solved as part of a SC with CIII (PDB IDs 6HU9, 6T15 and 6T0B), the monomeric CIV structure is missing Cox12, Cox13, Cox26 and Rcf2. The core of the map is resolved to a resolution better than 3.5 Å while some regions of the outer subunits were only resolved to 6–7 Å (Supplementary Fig. S2).

The map quality was sufficient to reliably model the nine subunits of CIV, including all prosthetic groups and several lipids, generating a molecular model with overall dimensions $125 \times 98 \times 70$ Å$^3$ and a molecular weight of 178 kDa (Fig. 1 and supplementary Fig. S4). The two haem A groups in Cox1 are well defined in the density as well as Cu$_B$ (Supplementary Fig. S4A). In addition, a Mg$^{2+}$ is present in Cox1, the dicopper Cu$_A$ centre is present in Cox2, as well as a Zn$^{2+}$ ion in Cox4. Surprisingly, the Ca$^{2+}$ ion [25] found in all previous Cox1 chains of yeast CIV structures in the SC form, is absent in this monomeric CIV. One of the residues typically associated with this ion, Glu39, adopts a different conformation, clearly visible in the map density, while no other conformational changes are observed in the region compared to the Ca$^{2+}$ bound structure (Fig. 2B). Six phospholipid molecules were modelled in the map as di-palmitoyl-3-SN-phosphatidylethanolamine (PEF). Precise identification of these lipids was not possible in places due to the limited density of these flexible lipids. These lipids are conserved with phospholipids found in the previous CIV containing SCs. However, compared to the previous yeast SC structures, the monomeric
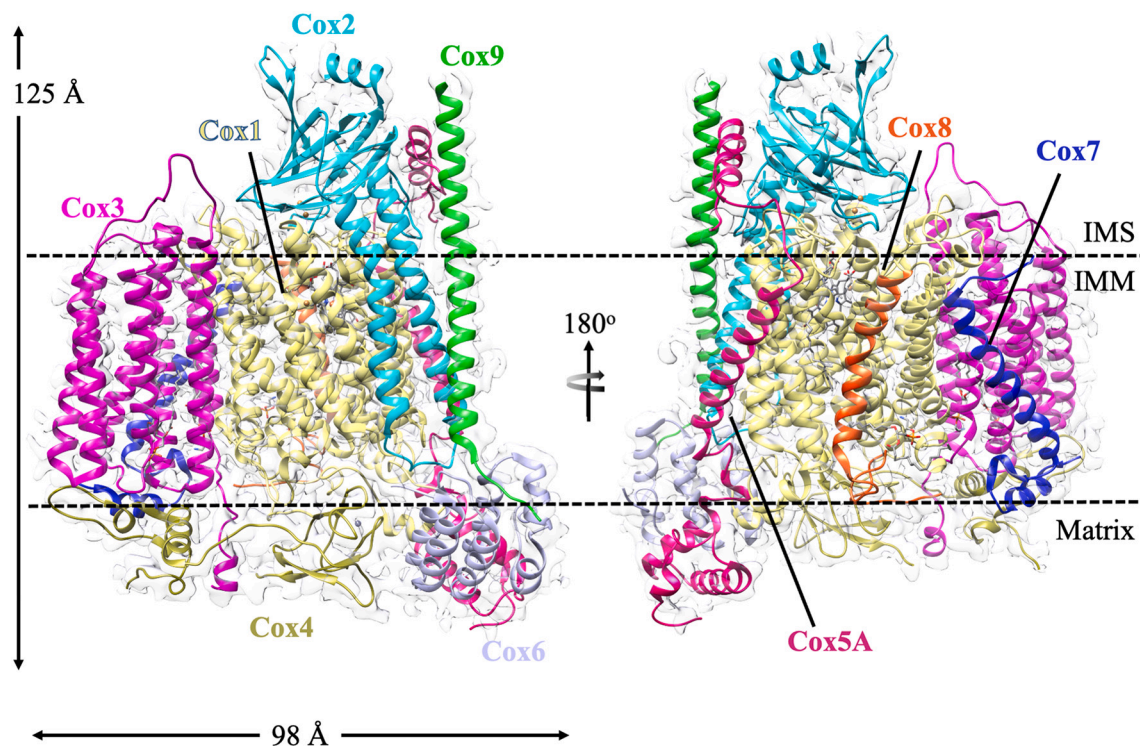


**Fig. 1.** Cryo-EM map and the fitted model in cartoon representation of the yeast monomeric CIV. The complex is shown in two different orientations of 180 degrees rotation over the y axis and the different proteins are colour coded as follows: Cox1: light yellow, Cox2: cyan, Cox3: magenta, Cox4: yellow, Cox5A: pink, Cox6: lilac, Cox7: blue, Cox8: orange, Cox9: green. The intermembrane space (IMS), the inner membrane (IMM) and the matrix are indicated to the right of the figure. Approximate dimensions of the complex are shown on the left. (For interpretation of the references to colour in this figure legend, the reader is referred to the web version of this article.)
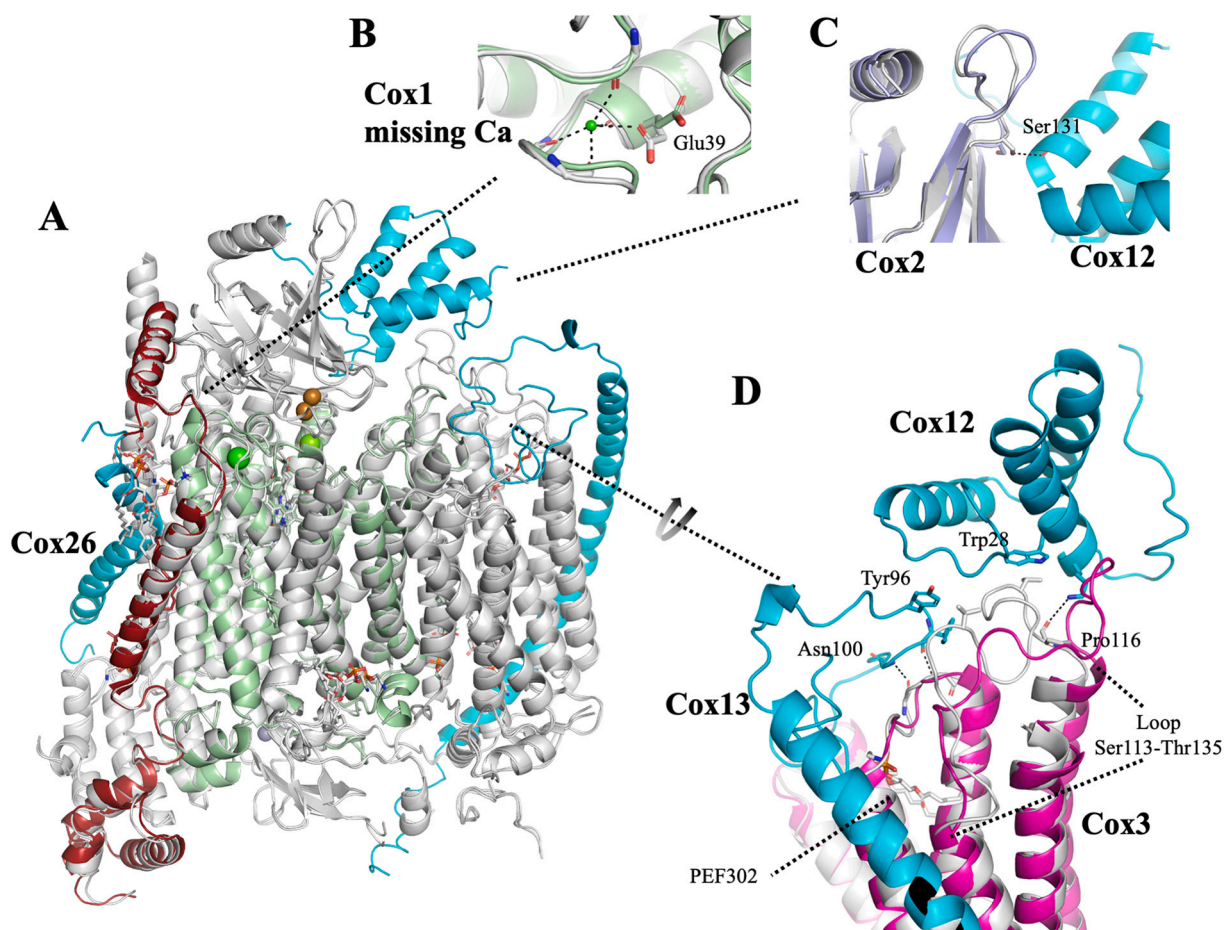
**Fig. 2.** Superposition of the yeast monomeric CIV to the CIV found in the yeast III-IV SC. (A) Superposition of the two structures. The missing subunits from the monomeric CIV are coloured in cyan (Cox13, Cox12 and Cox26). The rest of the CIV proteins from the SC assembly are coloured in grey. Cox5A of the monomeric CIV is coloured in red. (B) Structural details of the missing $Ca^{2+}$ in Cox1. No conformational changes are observed however the side chain of Glu29 is displaced. (C) Conformational changes of the Cox2 loop containing Ser131 in momomeric (light blue) and SC (grey) when interacting with Cox12 (cyan) in SC. (D) Conformational changes of Cox3 in monomeric (magenta) and SC (grey) when interacting with Cox13 (cyan) in the SC. (For interpretation of the references to colour in this figure legend, the reader is referred to the web version of this article.)

CIV has three fewer phospholipids. Two of the missing lipids were associated with the CIII-CIV interface in the SC, and the third interacted with Cox12 and Cox13, which are both missing in the monomeric structure of CIV (see below). As expected, no cardiolipin molecules were observed in the monomeric CIV since they are associated with CIII and with the CIII-CIV interface of SCs.

The CIV structure superimposes onto the CIV found in the $III_2-IV_2^{5A}$ SC (PDB ID 6HU9) with an overall RMSD value of 0.54 Å suggesting that the two CIV structures are virtually identical (Fig. 2A). The most notable deviations are observed in subunits that either interact with CIII in the SC or are in the proximity of the missing Cox12 and Cox13, as discussed below.

### 3.3. The role of Cox5A in CIV and supercomplex assembly

The yeast strain used in this study contained the genes coding for both Cox5 isoforms: Cox5A which is preferentially expressed in normoxic conditions of growth and Cox5B, expressed at low oxygen concentration. Both proteins were fitted into the cryo-EM map and examining the amino acids that are different in the two isoforms, we concluded that only Cox5A is present in CIV, consistent with other published SC structures obtained from cells grown in normoxia [8,26]. The map also excludes the possibility of both Cox5A and 5B being present in the complex, since there is no density supporting the side chains for the Cox5B residues Glu64, Phe97 and Phe104 (Supplementary Fig. S4C).

Cox5A is the sole subunit of CIV that interacts with CIII when present in a SC. Structural alignment of the two Cox5A chains (in monomeric and SC-associated CIV) suggests only minor differences with an RMSD of 0.8 Å, which is slightly higher than the CIV average (Fig. 3). Major differences appear at the N-terminal domain of the protein, where the Ala21-Ser43 region aligns with an RMSD of 1.4 Å. Visually, in the monomeric CIV the N-terminal domain appears to be closer to Cox6, whereas in the SC, the side chains of Asp33 and Asp48 are involved in electrostatic interactions with Qcr1 of CIII (Fig. 3C).

The central part of Cox5A comprising a transmembrane α-helix, is very similar in both monomeric and SC CIV. The N-terminus of this helix is identical in both structures despite the presence of a phospholipid in the SC only, which interacts with Qcr8 and Cyt1 of CIII and the cardiolipin CDL302 (Fig. 3). Minor differences appear in the hydrophobic sidechains of amino acids at the C-terminal end of the same α-helix. Here, in the SC CIV structure, a phospholipid (PCF202) is strongly bound to Cox5A and then *via* a second phospholipid (PEF607), interacts with Cox26 (Fig. 3A and central panel).

The C-terminus of Cox5A shows only minor differences between monomeric CIV and SC-bound CIV, mainly on the connecting loop with the central α-helix. Here, the side chains of Lys153 and Lys122, which are involved in interactions with the SC CIII chains Cyt1 and Qcr6 respectively, are adopting a less strained conformation in monomeric CIV (Fig. 3B).
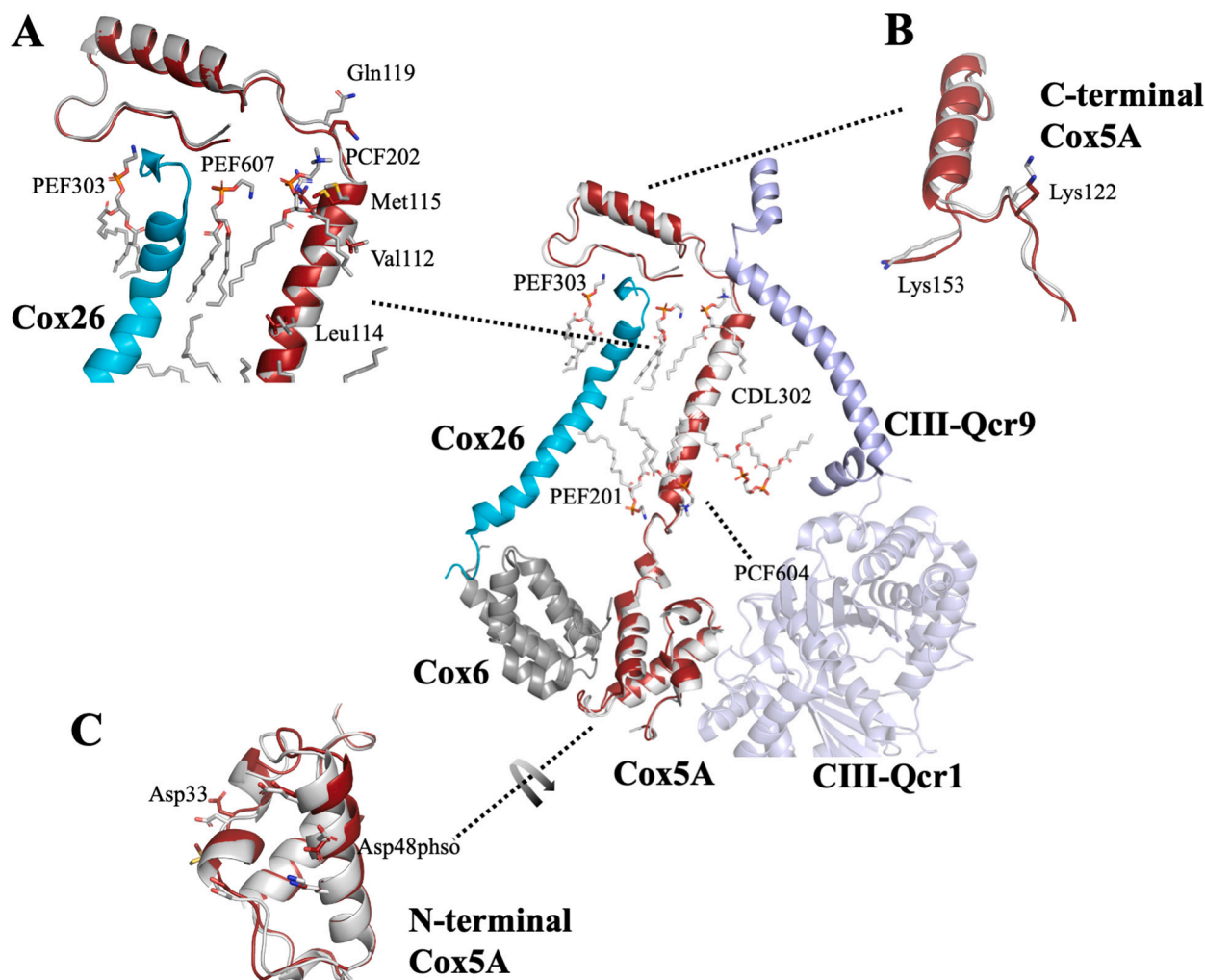
**Fig. 3.** Comparison of Cox5A in the monomeric CIV and the III-IV SC. Central panel: superposition of Cox5A in the monomeric CIV (in red) and the SC (in grey). The interacting CIII proteins are shown in light blue. Cox26, which is missing in the monomeric CIV structure, is coloured in cyan and Cox6 in dark grey. (A) The phospholipids PCF202, PEF607, and PEF303 (conserved in monomeric CIV) are involved in the Cox5A-Cox26 interaction of the SC. These are missing from the monomeric structure as well as the PEF201 and the cardiolipin CDL302 (central panel). (B) Superposition of the Cox5A C-termini. The two lysines involved in SC interactions are shown as sticks. (C) Conformational changes at the N-terminal of Cox5A during SC formation (in red the monomeric conformation). Residues involved in the interaction with CIII-Qcr1 are shown as sticks. (For interpretation of the references to colour in this figure legend, the reader is referred to the web version of this article.)

In conclusion, no major conformational changes can be seen in Cox5A when CIV is free from or associated to CIII in the SC. The differences at the N-terminus of the protein are minimal and CIII causes only a slight shift of the N-terminal domain, including a few side chain alterations that contribute to the SC formation. In addition, the lipids found between CIV and CIII in the SC don't seem to affect Cox5A assembly. The most striking differences are found in the interaction of Cox5A with Cox26 within the SC-bound CIV. It is possible that Cox26 plays an integral part in SC formation through a network of phospholipids that extends from Cox26 up to the interface with CIII.

### 3.4. Conformational changes in Cox2 and Cox3 due to the missing Cox12 and Cox13

The largest differences between the monomeric and the SC-bound CIV are found in the distal part of CIV, far from Cox5 and the CIII-interface of the SC. Here, Cox12 and Cox13 are completely missing from the monomeric CIV and as a result, conformational changes are observed in the neighbouring subunits, Cox2 and Cox3 (Fig. 2C & D). While the central β-barrel of Cox2 remains unchanged in both structures, a loop connecting two of the barrel β-strands (Cox2 residues 130–141)

displays large deviations between the two structures, reaching up to 3.7 Å as main chain atom distances. In addition, the position of Ser131, which interacts with the carbonyl of Asp56 in Cox12 in the SC, is now adopting a different conformation, suggesting that Ser131 is a key residue involved in the Cox2-Cox12 interaction that is missing in the monomeric CIV.

Larger conformational changes are observed in Cox3, specifically on the intermembrane space (IMS) side with the loss of the interactions with Cox12 and Cox13 in the monomeric CIV. The main electrostatic interactions between Cox3 and Cox13 in the SC are observed between the residues Ser197 and Gly199 in Cox3, and Asn100 and Phe98 in Cox13 (Fig. 2D). However, as this loop in Cox3 is structurally conserved in both structures, a possible disruption of the interface might be due to the loss of the lipid PEF302 that mediates the interaction between Cox3 and the C-terminus of Cox13 in the SC. The loss of Cox13 results in larger conformational changes in another loop of Cox3 (Ser115-Thr135). Hydrophobic interactions between Val27 of Cox3 and Tyr96 and Phe98 of Cox13, and between Val118 of Cox3 with Trp28 of Cox12, are now missing, as is the hydrogen bond between the Pro116 of Cox3 and Lys25 of Cox12 (Fig. 2C). As a result, when compared to the SC CIV, the loop in the monomeric CIV displays higher B-factors and lower resolution

(Supplementary fig. S2C & B).

In conclusion, the loss of Cox12 and Cox13 from CIV appears to correlate with the loss of a phospholipid. It is difficult to assess at what stage those subunits have been lost. It could be at the solubilisation stage were membranes were exposed to the highest detergent concentration. However, the six-histidine-tag subsequently exploited for affinity chromatography is at the C-terminus of Cox13 so unless that step was non-specific, one would expect Cox13 to be part of the enzyme after Ni-affinity elution. The turnover number of CIV in the nickel-eluate was measured at $125 \pm 17$ e.s$^{-1}$. This is 30 % lower than other monomeric CIV preparations performed from the same yeast strain [13], a difference that may reflect the loss of supernumerary subunits.

Finally, there is no density for an Rcf protein in the cryo-EM map of monomeric CIV where Rcf2 was previously observed in SCs [7]. This may also be due to missing Cox12 and Cox13, proteins that together with Cox3 were shown to interact with Rcf2.

*3.5. Yeast and bovine CIV*

The monomeric CIV displays high similarities to the mammalian CIVs. To date, the only available eukaryotic structure of CIV that is not part of a SC assembly is the bovine CIV from heart mitochondria, determined by X-ray crystallography. Among all the structures of the bovine CIV, the only monomeric CIV structure was only recently reported at a resolution of 1.9 Å [5]. Superposition of this structure (fully oxidised PDB ID 6JY3) with the yeast CIV reveals an RMSD of 1.1 Å suggesting a very similar conformation. The major differences appear at the N-termini of the yeast Cox5A/bovine COX4 pair, as well as in the yeast Cox4/bovine COX5B pair (Fig. 4). Apart from the missing Cox13 and Cox12 in the yeast monomeric CIV structure (corresponding to bovine COX6A and COX6B) for reasons which are most likely linked to our purification protocol and the use of maltoside, only bovine COX7B and COX8B have no equivalent in yeast *S. cerevisiae* CIV [12] (Fig. 4).

## 4. Conclusions

Association of respiratory complexes in SCs has attracted a lot of interest in the field of bioenergetics and several structural models at near atomic resolution have been published that have contributed to developing our understanding of the role and assembly process of those SCs. In the yeast *S. cerevisiae*, that lacks CI, only III-IV SCs have been identified. Structures of the III$_2$-IV$_1$ and III$_2$-IV$_2$ SCs have been determined at high resolution [6–8] and whether one or two CIVs associate to CIII was shown to correlate with the level of expression of CIV in the yeast inner mitochondrial membrane [7], with no other difference than the CIII:CIV stoichiometry in the CIII-CIV interaction.

Evidences for a functional kinetic advantage of the yeast III-IV SCs have also been shown to reside in the 2D diffusion of cytochrome *c* at the IMS surface of the III-IV SC [27]. This was concluded from a combination of activity assays and cryo-EM structures of the yeast SCs with cytochrome *c*, and complemented previous studies where CIII mutants were created to effectively prevent SC formation [8].

When and how SCs are formed might be the area of lowest understanding in *S. cerevisiae* and one reason for that might be that the biogenesis of individual complexes and of SCs are not independent. Recent structures of the mammalian III-IV SCs have revealed that the mechanism of SC formation is mediated by SCAF1 [10], one of three mammalian COX7A homologues that are found at the interface of SCs. No such mechanism has to date been proposed for the formation of the yeast or plant III-IV SC and it is noteworthy that the CIII:CIV interface is formed by a different CIV subunit in these species [6,7,9,10,26], indicating that SCs might have evolved separately. Curiously however, in all organisms sampled so far, the CIV subunits at the CIII:CIV interface involve 'accessory' subunits with differentially expressed isoforms (in yeast, Cox5 is the only accessory subunit with isoforms) and the full implications of this observation is yet to be understood. In yeast, structural studies on Cox5 isoforms didn't reveal any major change in the
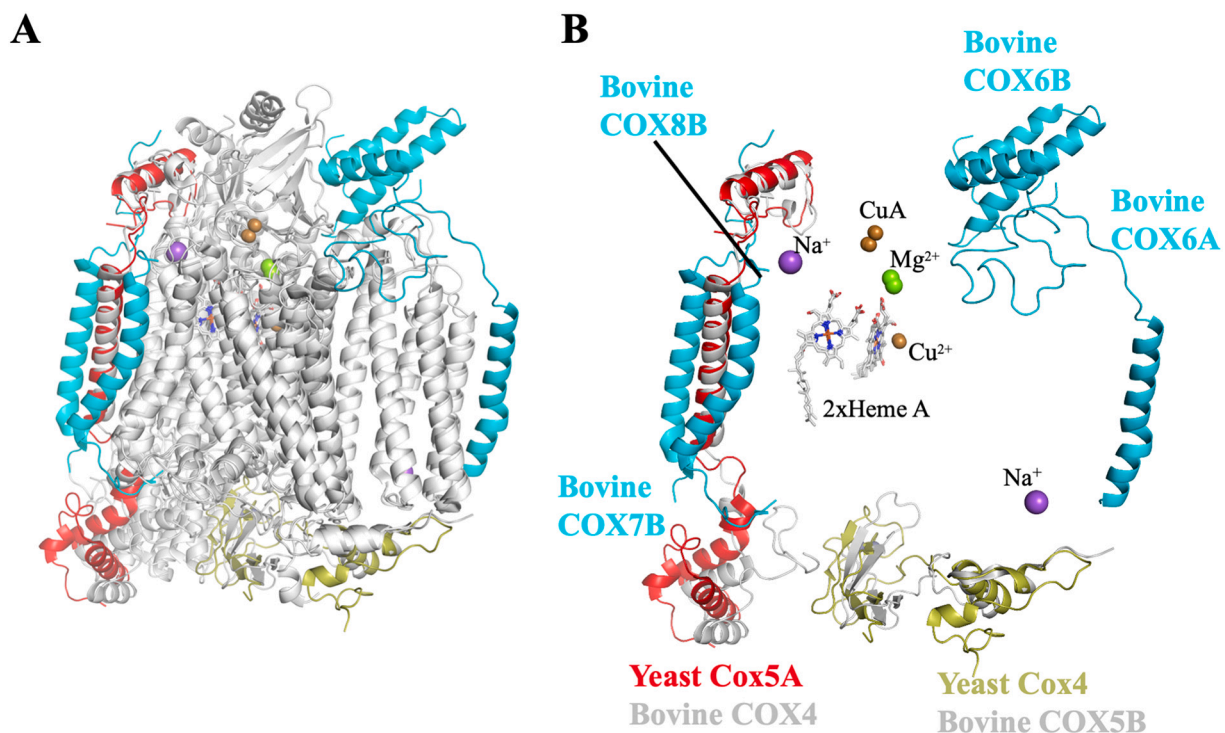


**Fig. 4.** Superposition of the monomeric yeast CIV to the monomeric CIV from bovine heart (PDB ID: 6JY3). (A) Superposition of the two CIVs. The extra domains found in the bovine structure are shown in cyan. Domains with large conformational changes are coloured for the yeast structure: Cox5A in red and Cox4 in light brown. (B) Highlights of major conformational differences between the two structures: Cox5A/COX4, Cox4/COX5B and missing proteins from yeast CIV. Chains are colour coded as in panel A. The dicopper Cu$_A$ centre, the two heme A, the Cu$_B$ (Cu$^{2+}$) and Mg$^{2+}$ are all conserved whereas the two Na$^+$ ions are missing from the yeast monomeric structure. (For interpretation of the references to colour in this figure legend, the reader is referred to the web version of this article.)

architecture of their associated SCs [7].

Yeast Rcf proteins Rcf1 and Rcf2 had first been proposed to be SC assembly factors but recent studies have shown, convincingly, that they would be best described as CIV assembly factors and even more likely, in the case of Rcf2, as a constitutive subunit of CIV following post-translational cleavage of the full-length protein [7,28]. No Rcf protein was detected in the present work, nor were Cox12 and Cox13 which are late CIV assembly subunits of the Cox3 module [29], maybe indicating SC formation before CIV is fully assembled itself. This highlights another obstacle to our understanding of these complexes, the fact that any biochemical or biophysical characterisation that involves isolation of the SC or individual complexes may not be representative of the native, *in situ* state of the protein assembly of interest. A similar question persists in mammalian systems where the CIV subunit NDUFA4, which is not homologous to Rcf2 but locates in the same region of CIV, has only been observed so far in the human CIV structure as part of a SC [2]. This has led to a proposal that CIV subunit number (in addition to isoform type) may vary depending on CIV membrane organisation as for instance, the presence of NDUFA4 would preclude CIV dimerization.

Here we showed that, as in mammalian systems, the yeast mono-meric CIV maintains a rather rigid core conformation that remains intact when it is in a SC. It is noteworthy that the presented structure may not reflect this of CIV independently assembling and accumulating in absence of CIII as the monomeric enzyme was generated artificially using detergents that separated it from CIII. The conditions for isolation resulted in the loss of subunits which highlighted the importance of lipids in maintaining enzyme integrity and SC formation.

## Data availability

All relevant data are included in the manuscript and/or are available from the corresponding author upon reasonable request. The cryo-EM map of monomeric CIV has been deposited in the Electron Microscopy Data Bank under accession code EMD-14436. The coordinates of the atomic model of monomeric CIV have been deposited in the Protein Data Bank under accession code PDB ID 7Z10.

## Declaration of competing interest

The authors declare that they have no known competing financial interests or personal relationships that could have appeared to influence the work reported in this paper.

## Data availability

Data will be made available on request.

### Author contributions

A.M. designed and supervised the research. A.M.H. did the protein and microscopy work. G.I. and N.P. processed the cryo-EM images and built the model. All authors wrote the manuscript.

## Appendix A. Supplementary data

Supplementary data to this article can be found online at https://doi.org/10.1016/j.bbabio.2022.148591.

## References

[1] P.R. Rich, A. Maréchal, Electron transfer chains: structures, mechanisms and energy coupling, in: S.J. Ferguson (Ed.), Comprehensive Biophysics, Comprehensive Biophysics, vol. 8, Elsevier Academic Press Inc, San Diego, 2012, pp. 72–93.

[2] S. Zong, M. Wu, J. Gu, T. Liu, R. Guo, M. Yang, Structure of the intact 14-subunit human cytochrome c oxidase, Cell Res. 28 (2018) 1026–1034.

[3] B. Kadenbach, Complex IV – the regulatory center of mitochondrial oxidative phosphorylation, Mitochondrion 58 (2021) 296–302.

[4] T. Tsukihara, H. Aoyama, E. Yamashita, T. Tomizaki, H. Yamaguchi, K. Shinzawa-Itoh, R. Nakashima, R. Yaono, S. Yoshikawa, The whole structure of the 13-subunit oxidized cytochrome c oxidase at 2.8 Å, Science 272 (1996) 1136–1144.

[5] K. Shinzawa-Itoh, T. Sugimura, T. Misaki, Y. Tadehara, Y. Yamamoto, M. Hanada, N. Yano, T. Nakagawa, S. Uene, T. Yamada, H. Aoyama, E. Yamashita, T. Tsukihara, S. Yoshikawa, K. Muramoto, Monomeric structure of an active form of bovine cytochrome c oxidase, Proc. Natl. Acad. Sci. U. S. A. 116 (2019) 19945–19951.

[6] A.M. Hartley, N. Lukoyanova, Y. Zhang, A. Cabrera-Orefice, S. Arnold, B. Meunier, N. Pinotsis, A. Maréchal, Structure of yeast cytochrome c oxidase in a supercomplex with cytochrome bc1, Nat. Struct. Mol. Biol. 26 (2019) 78–83.

[7] A.M. Hartley, B. Meunier, N. Pinotsis, A. Maréchal, Rcf2 revealed in cryo-EM structures of hypoxic isoforms of mature mitochondrial III-IV supercomplexes, Proc. Natl. Acad. Sci. U. S. A. 117 (2020) 9329–9337.

[8] J. Berndtsson, A. Aufschnaiter, S. Rathore, L. Marin-Buera, H. Dawitz, J. Diessl, V. Kohler, A. Barrientos, S. Büttner, F. Fontanesi, M. Ott, Respiratory supercomplexes enhance electron transport by decreasing cytochrome c diffusion distance, EMBO Rep. 21 (2020).

[9] M. Maldonado, J.A. Letts, Guo Fei, Atomic structures of respiratory complex III2, complex IV, and supercomplex III2-IV from vascular plants, elife (2021) 9, e56664.

[10] I. Vercellino, L. Sazanov, Structure and assembly of the mammalian mitochondrial supercomplex CIII2CIV, Nature 598 (2021) 364–367.

[11] J.P. Lasserre, A. Dautant, R.S. Aiyar, R. Kucharczyk, A. Glatigny, D. Tribouillard-Tanvier, J. Rytka, M. Blondel, N. Skoczen, P. Reynier, L. Pitayu, A. Rötig, A. Delahodde, L.M. Steinmetz, G. Dujardin, V. Procaccio, J.P. di Rago, Yeast as a system for modeling mitochondrial disease mechanisms and discovering therapies, Dis. Model. Mech. 8 (2015) 509–526.

[12] A. Maréchal, B. Meunier, D. Lee, C. Orengo, P.R. Rich, Yeast cytochrome c oxidase: a model system to study mitochondrial forms of the haem-copper oxidase superfamily, Biochim. Biophys. Acta 2012 (1817) 620–628.

[13] B. Meunier, A. Maréchal, P.R. Rich, Construction of histidine-tagged yeast mitochondrial cytochrome c oxidase for facile purification of mutant forms, Biochem. J. 444 (2012) 199–204.

[14] S.Q. Zheng, E. Palovcak, J.P. Armache, K.A. Verba, Y. Cheng, D.A. Agard, MotionCor2: anisotropic correction of beam-induced motion for improved cryo-electron microscopy, Nat. Methods 14 (2017) 331–332.

[15] J. Zivanov, T. Nakane, S.H.W. Scheres, Estimation of high-order aberrations and anisotropic magnification from cryo-EM data sets in RELION-3.1, IUCrJ 7 (2020) 253–267.

[16] A. Punjani, J.L. Rubinstein, D.J. Fleet, M.A. Brubaker, cryoSPARC: algorithms for rapid unsupervised cryo-EM structure determination, Nat. Methods 14 (2017) 290–296.

[17] A. Rohou, N. Grigorieff, CTFFIND4: fast and accurate defocus estimation from electron micrographs, J. Struct. Biol. 192 (2015) 216–221.

[18] D. Liebschner, P.V. Afonine, M.L. Baker, G. Bunkóczi, V.B. Chen, T.I. Croll, B. Hintze, L.W. Hung, S. Jain, A.J. McCoy, N.W. Moriarty, R.D. Oeffner, B.K. Poon, M.G. Prisant, R.J. Read, J.S. Richardson, D.C. Richardson, M.D. Sammito, O. V. Sobolev, D.H. Stockwell, T.C. Terwilliger, A.G. Urzhumtsev, L.L. Videau, C. J. Williams, P.D. Adams, Macromolecular structure determination using X-rays, neutrons and electrons: recent developments in phenix, Acta Crystallogr D Struct Biol. 75 (2019) 861–877.

[19] P. Emsley, B. Lohkamp, W.G. Scott, K. Cowtan, Features and development of coot, Acta Crystallogr. Sect. D Biol. Crystallogr. 66 (2010) 486–501.

[20] L. Schrödinger, PyMOL: The PyMOL Molecular Graphics Syster, Version 2.0, 2015.

[21] E. Krissinel, K. Henrick, Secondary-structure matching (SSM), a new tool for fast protein structure alignment in three dimensions, Acta Crystallogr. Sect. D 60 (2004) 2256–2268.

[22] E.F. Pettersen, T.D. Goddard, C.C. Huang, G.S. Cough, D.M. Greenblatt, E.C. Meng, T.E. Ferrin, UCSF Chimera–a visualization system for exploratory research and analysis, J. Comput. Chem. 25 (2004) 1605–1612.

[23] M. Zoonens, J.-L. Popot, Amphipols for each season, J. Membr. Biol. 247 (2014) 759–796.

[24] J.A. Letts, K. Fiedorczuk, G. Degliesposti, M. Skehel, L.A. Sazanov, Structures of respiratory supercomplex I+III 2 reveal functional and conformational crosstalk, Mol. Cell 75 (2022) 1131–1146.

[25] A. Maréchal, M. Iwaki, P.R. Rich, Structural changes in cytochrome c oxidase induced by binding of sodium and calcium ions: an ATR-FTIR study, J. Am. Chem. Soc. 135 (2013) 5802–5807.

[26] S. Rathore, J. Berndtsson, L. Marin-Buera, J. Conrad, M. Carroni, P. Brzezinski, M. Ott, Cryo-EM structure of the yeast respiratory supercomplex, Nat. Struct. Mol. Biol. 26 (2019) 50–57.

[27] A. Moe, J. Di Trani, J.L. Rubinstein, P. Brzezinski, Cryo-EM structure and kinetics reveal electron transfer by 2D diffusion of cytochrome c in the yeast III-IV respiratory supercomplex, in: Pro. Natl. Acad. Sci. U. S. A. 118, Pro. Natl. Acad. Sci. U. S. A., 118, 2021.

[28] K. Römpler, T. Müller, L. Juris, M. Wissel, M. Vukotic, K. Hofmann, M. Deckers, Overlapping role of respiratory supercomplex factor Rcf2 and its N-terminal homolog Rcf3 in Saccharomyces cerevisiae, J. Biol. Chem. 291 (2016) 23769–23778.

[29] A. Timón-Gómez, E. Nývltová, L.A. Abriata, A.J. Vila, J. Hosler, A. Barrientos, Mitochondrial cytochrome c oxidase biogenesis: recent developments, Semin. Cell Dev. Biol. 76 (2018) 163–178.